REPORT DOCUMENTATION PAGE

Form Approved OMB NO. 0704-0188

1. REPORT DATE (DD-MM-YYYY)	2. REPORT TYPE	3. DATES COVERED (From - To)
23-09-2022	Final Report	1-May-2017 - 30-Apr-2022

4. TITLE AND SUBTITLE
Final Report: Extreme Dissipation Behavior of Main-Chain Liquid-Crystal Elastomers and Structures

5a. CONTRACT NUMBER
W911NF-17-1-0165

5b. GRANT NUMBER

5c. PROGRAM ELEMENT NUMBER
611102

6. AUTHORS

5d. PROJECT NUMBER

5e. TASK NUMBER

5f. WORK UNIT NUMBER

7. PERFORMING ORGANIZATION NAMES AND ADDRESSES
Johns Hopkins University
3400 North Charles Street
Malone 146
Baltimore, MD 21218 -2608

8. PERFORMING ORGANIZATION REPORT NUMBER

9. SPONSORING/MONITORING AGENCY NAME(S) AND ADDRESS (ES)
U.S. Army Research Office
P.O. Box 12211
Research Triangle Park, NC 27709-2211

10. SPONSOR/MONITOR'S ACRONYM(S)
ARO

11. SPONSOR/MONITOR'S REPORT NUMBER(S)
70188-SM.4

12. DISTRIBUTION AVAILIBILITY STATEMENT
Approved for public release; distribution is unlimited.

13. SUPPLEMENTARY NOTES
The views, opinions and/or findings contained in this report are those of the author(s) and should not contrued as an official Department of the Army position, policy or decision, unless so designated by other documentation.

14. ABSTRACT

15. SUBJECT TERMS

16. SECURITY CLASSIFICATION OF:			17. LIMITATION OF ABSTRACT	15. NUMBER OF PAGES	19a. NAME OF RESPONSIBLE PERSON
a. REPORT	b. ABSTRACT	c. THIS PAGE			Thao Nguyen
UU	UU	UU	UU		19b. TELEPHONE NUMBER 410-516-4528

RPPR Final Report
as of 04-Oct-2022

Agency Code: 21XD

Proposal Number: 70188SM **Agreement Number: W911NF-17-1-0165**
INVESTIGATOR(S):

Name: Thao Nguyen
Email: Vicky.Nguyen@jhu.edu
Phone Number: 4105164528
Principal: Y

Organization: **Johns Hopkins University**
Address: 3400 North Charles Street, Baltimore, MD 212182608
Country: USA
DUNS Number: 001910777 EIN: 520595110

Report Date: 31-Jul-2022 Date Received: 23-Sep-2022
Final Report for Period Beginning 01-May-2017 and Ending 30-Apr-2022
Title: Extreme Dissipation Behavior of Main-Chain Liquid-Crystal Elastomers and Structures
Begin Performance Period: 01-May-2017 **End Performance Period:** 30-Apr-2022
Report Term: 0-Other

Submitted By: Thao Nguyen Email: Vicky.Nguyen@jhu.edu
Phone: (410) 516-4528

STEM Degrees: **STEM Participants:**

Major Goals: The goal of this project is to develop a fundamental understanding of the relaxation mechanisms of main-chain LCEs to enable the design of extraordinary dissipation behaviors of LCE materials and structures over multiple length scales. We hypothesize that the enhanced dissipation behavior of LCEs arise from the coupling of the relaxation dynamics of the mesogens and polymer network, and depends on the mesogen order and chain alignment. Furthermore, the intrinsic dissipation behavior can be exploited in an architected design to produce structures with extreme damping and energy absorption. The aims of the proposed work are:

Aim 1 Synthesize and characterize main-chain networks with tailored chain alignment and mesogen order

Aim 2: Characterize the anisotropic relaxation behavior of the mesogens and polymer network using wide-angle X-ray scattering and LCEs with tailored structures.

Aim 3: Develop a nonlinear thermoviscoelasticity theory for LCEs.

Aim 4: Design, fabricate and characterize architected LCE structures.

Accomplishments: At the end of the fourth (final) year, we completed Aims 1 - 4. The outcomes for the Aims have been described in the prior years' annual progress reports and published in archival journals. The report in the uploaded PDF collates the main results of the project described in previous years' reports.

Training Opportunities: This grant partly funded and provided research projections for 4 Ph.D. students: Nicholas Traugutt (CU Denver), Risheng Zhou, Zhejiang Wang (JHU), Beijun Shen (JHU). It also partly funded a Masters of Science student, Cristina Martin Linares (JHU), and a postdoctoral fellow, Seung-Yeol Jeon (JHU). Dr. Traugutt graduated and is now working at a startup for the 3D printing of LCEs. Zheliang Wang also graduated and is not a postdoc at UT Austin. Dr. Jeon is a research scientist at the Korea Institute of Science and Technology. Ms. Beijun Shen is a 4 year Ph.D. student.

The effort listed in the Participants section is for the period 9/1/2021-4/30/2022.

RPPR Final Report
as of 04-Oct-2022

Results Dissemination: Publications

1. Z. Wang, A. El Hajj Chebade, S. Govindjee, T. D. Nguyen, “A nonlinear viscoelasticity theory for nematic liquid crystal elastomers”, Journal of the Mechanics and Physics of Solids (2022), 163, 104829

2. S. Jeon, B. Shen, N. A. Traugutt, Z. Zhu, C. M. Linares, O.-C. Kwon, T. D. Nguyen, C. Yakacki, S. H. Kang, “Strain rate-adaptive extreme energy ab-sorption via architected liquid-crystalline elastomers", Advanced Materials (2022), 34, 2200272.

3. Mistry, D., Traugutt, N. A., Sanborn, B., Volpe, R. H., Chatham, L., Zhou, R., ... & Yakacki, C. M. (2021). Soft-Elasticity Optimizes Dissipation in 3D-Printed Liquid Crystal Elastomers. arXiv preprint arXiv:2106.02165.

4. C. P. Martin Linares, N. A. Traugutt, M. Saed, A. Martin Linares, C. M. Yakacki, T. D. Nguyen, “The effect of alignment on the rate-dependent behavior of a main-chain liquid crystal elastomers", Soft Matter (2020), 16, 8782-8798.

5. Luo, C., Chung, C., Traugutt, N. A., Yakacki, C. M., Long, K. N., & Yu, K. (2020). 3D Printing of Liquid Crystal Elastomer Foams for Enhanced Energy Dissipation Under Mechanical Insult. ACS Applied Materials & Interfaces, 13(11), 12698-12708.

6. Traugutt, N. A., Mistry, D., Luo, C., Yu, K., Ge, Q., & Yakacki, C. M. (2020). Liquid?crystal?elastomer?based dissipative structures by digital light processing 3D printing. Advanced Materials, 32(28), 2000797.

7. S.-Y. Jeon, S. H. Kang, “Electrochemical reactions drive morphing of materials,” Nature, (2019),573, 198-199.

8. Merkel DR, Traugutt NA, Visvanathan R, Yakacki CM, Frick CP, “Thermomechanical properties of monodomain nematic main-chain liquid crys-tal elastomers” Soft Matter (2018), 14(29), pp. 6024-6036.

9. Hanzon D, Traugutt NA, McBride M, Bowman CN, Yakacki CM, Yu K, “Adaptable Liquid Crystal Elastomers with Transesterification-Based Bond Ex-change Reactions” Soft Matter (2018), 14, 951-960.

10. Ula SW, Traugutt NA, Volpe RH, Patel RR, Yu K, Yakacki CM, “Liquid Crystal Elastomers: An Introduction and Review of Emerging Technolo-gies” Liquid Crystals Reveiws, (2018), 6 (1), pp 78-107.

Presentations

T. D. Nguyen “Viscoelastic Behavior of Main Chain Liquid Crystal Elastomers ", Plenary,18th Mechanics of Materials Conferences, Oxford University, UK, 4/5/2022.

T. D. Nguyen, “Viscoelastic Behavior of Main Chain Liquid Crystal Elastomers," ETH Soft Materials Group Meeting, ETH, 6/9/2021.

T. D. Nguyen “Viscoelastic Behavior of Main Chain Liquid Crystal Elastomers ", MEC Caltech Seminar Series, Caltech, 4/22/2021.

H. Kang, “Self-adaptive materials, structures and programmable materials,” Air Force Research Laboratory, Dayton, OH, August 2021. (invited)

S. H. Kang, “Architected Liquid Crystalline Elastomers with Strain Rate-Adaptive Extreme Energy Absorption,” 2021 Spring Materials Research Socie-ty Meeting (Virtual), April 2021.

S. H. Kang, “Mechanical Metamaterials with Strain-Rate Adaptive Energy Ab-sorption,” 2021 American Physical Society March Meeting (Virtual), March 2021.

S. H. Kang, “Self-adaptive materials, structures and devices,” Department of Mechanical and Aerospace Engineering, Ohio State University, Columbus, OH, February 2021. (invited)

S. H. Kang, “Self-adaptive materials, structures and devices,” Department of Mechanical Engineering, Villanova University, Villanova, PA, November 2020. (invited)

S. Jeon, Z. Zhu, N. Traugutt, B. Shen, T. D. Nguyen, C. M. Yakacki, and S. H. Kang, “Extreme Energy Absorbing Architected Materials Based on Liquid Crystal Elastomers,” American Society of Mechanical Engineers International Mechanical Engineering Congress and Exposition (Virtual), November 2020.

S. H. Kang, “Architected materials with adaptive energy absorption and bioin-spired self-adaptable materials & medical devices,” Department of Mechanical Engineering, University of Wisconsin, Madison, WI, October 2020. (invited)

S. Jeon, Z. Zhu, N. Traugutt, B. Shen, T. D. Nguyen, C. M. Yakacki, and S. H. Kang, “Extreme energy absorbing architected materials based on liquid crystal elastomer structures,” Society of Engineering Science Annual Meeting (Virtual Live Talk), September 2020.

S. H. Kang, “Self-adaptive materials, structures and devices,” Air Force Research Laboratory, Dayton, OH, July 2020. (invited)

S. H. Kang, “Architected materials with adaptive energy absorption and bioinspired self-adaptable materials & medical devices,” School of Mechanical Engineering, Georgia Institute of Technology, Atlanta, GA, February 2020. (invited)

S. H. Kang, “Architected materials with adaptive energy absorption and bioinspired self-adaptable materials,” Department of Mechanical Engineering, Massachusetts Institute of Technology, Cambridge, MA, February 2020. (invited)

S. H. Kang, “Architected materials with adaptive energy absorption and bioinspired self-adaptable materials,” Department of Mechanical Engineering, University of South Carolina, Columbia, SC, February 2020. (invited)

S. H. Kang, “Architected materials with adaptive energy absorption and bioinspired self-adaptable materials,” Department of Mechanical Engineering, University of Utah, Salt Lake City, UT, November 2019. (invited)

S. H. Kang, “Architected materials with adaptive energy absorption and bioinspired self-adaptable materials,” Department of Mechanical Engineering, McGill University, Montreal, Canada, October 2019. (invited)

S. H. Kang, “Architected materials with adaptive energy absorption and bioinspired self-adaptable materials,” School of Mechanical Engineering, Purdue University, West Lafayette, IN, September 2019. (invited)

S. H. Kang, “Metamaterials with adaptive energy absorption and bioinspired self-adaptable materials,” Department of Physics, University of North Texas, Dallas, TX, September 2019. (invited)

S. Jeon, Z. Zhu, C. M. Yakacki, T. D. Nguyen, and S. H. Kang, “Extreme impact energy absorption behaviors of liquid crystal elastomer structures,” ASME International Mechanical Engineering Congress and Exposition, Salt Lake City, UT, November 2019.

S. Jeon, Z. Zhu, C. M. Yakacki, T. D. Nguyen, and S. H. Kang, “Extreme impact energy trapping metamaterials based on liquid crystal elastomers,” 56 Annual Technical Meeting of the Society of Engineering Science, St. Louis, MO, October 2019.

Honors and Awards: 2020 Johns Hopkins University Catalyst Award (co-PI Sung Hoon Kang)

2020 Air Force Summary Faculty Fellowship (co-PI Sung Hoon Kang)

2019 ASME Applied Mechanics Division Haythornthwaite Foundation Student Travel Award (PhD Student Lichen Fang)

Protocol Activity Status:

RPPR Final Report
as of 04-Oct-2022

Technology Transfer: 2021 Subaward PI, Chris Yakacki, was awarded a small business development contract (W911QY21C0038) from DoD-Army-AMC to develop a lattice system embedded with liquid-crystal elastomers that could fitted into an extreme combat helmet.

In 2020, Co-PI Kang and PI Nguyen are collaborating with Drs. Robert Haynes and Todd Henry of ARL in Aberdeen Proving Ground, regarding understanding vibration dissipation behaviors of liquid crystalline elastomers.

PARTICIPANTS:

Participant Type: PD/PI
Participant: Thao D Nguyen
Person Months Worked: 1.00 **Funding Support:**
Project Contribution:
National Academy Member: N

Participant Type: Co PD/PI
Participant: Christopher Yakacki
Person Months Worked: 1.00 **Funding Support:**
Project Contribution:
National Academy Member: N

Participant Type: Graduate Student (research assistant)
Participant: Rhiseng Zhou
Person Months Worked: 3.00 **Funding Support:**
Project Contribution:
National Academy Member: N

International Travel:

GBR 3 days

ARTICLES:

RPPR Final Report
as of 04-Oct-2022

Publication Type: Journal Article Peer Reviewed: Y **Publication Status:** 1-Published
Journal: Soft Matter
Publication Identifier Type: DOI Publication Identifier: 10.1039/C7SM02110K
Volume: 14 Issue: 6 First Page #: 951
Date Submitted: 10/8/18 12:00AM Date Published: 2/14/18 3:00PM
Publication Location:
Article Title: Adaptable liquid crystal elastomers with transesterification-based bond exchange reactions
Authors: Drew W. Hanzon, Nicholas A. Traugutt, Matthew K. McBride, Christopher N. Bowman, Christopher M. Y
Keywords: LCE, bond exchange reactions, mesogen
Abstract: Adaptable liquid crystal elastomers (LCEs) have recently emerged to provide a new and robust method to program monodomain LCE samples. When a constant stress is applied with active bond exchange reactions (BERs), polymer chains and mesogens gradually align in the strain direction. Mesogen alignment is maintained after removing the BER stimulus (e.g. by lowering the temperature) and the programmed LCE samples exhibit free-standing two-way shape switching behavior. Here, a new adaptable main-chain LCE system was developed with thermally induced transesterification BERs. The network combines the conventional properties of LCEs, such as an isotropic phase transition and soft elasticity, with the dynamic features of adaptable network polymers, which are malleable to stress relaxation due to the BERs. Polarized Fourier transform infrared measurements confirmed the alignment of polymer chains and mesogens after strain-induced programming. The influence of the creep stress, temperature, and t
Distribution Statement: 3-Distribution authorized to U.S. Government Agencies and their contractors
Acknowledged Federal Support: **Y**

Publication Type: Journal Article Peer Reviewed: Y **Publication Status:** 1-Published
Journal: Liquid Crystals Reveiws
Publication Identifier Type: DOI Publication Identifier: 10.1080/21680396.2018.1530155
Volume: 6 Issue: 1 First Page #: 78
Date Submitted: 10/8/18 12:00AM Date Published: 8/1/19 4:00AM
Publication Location:
Article Title: Liquid Crystal Elastomers: An Introduction and Review of Emerging Technologies
Authors: Sabina W. Ula, Nicholas A. Traugutt, Ross H. Volpe, Ravi R. Patel, Kai Yu and Christopher M. Yakacki
Keywords: Liquid crystal elastomer; main-chain LCE; click chemistry; covalent adaptable network; 4D printing
Abstract: Liquid crystal elastomers (LCEs) are a unique class of materials that combine rubber elasticity with liquid crystalline anisotropy to produce exceptional physical and optical properties such as actua- tion, soft elasticity, and birefringence. This review gives a brief overview of the physics behind liquid crystals and classifications of LCEs before discussing the methods traditionally used to synthesize LCEs, the new methods of synthesis that have emerged within the past several years, and the developing applications of LCEs. The review begins by discussing the organization of liquid crystals in LCEs and how their coupling to the polymer backbone affects their macroscopic properties. Tradi- tional LCE synthesis methods and their drawbacks in terms of moving towards applications are then touched upon, as well as emerging chemistries that eliminate many of the challenges associated with LCE synthesis. Thiol-Michael reactions and covalent adaptable networks, which allow for bulk sam-
Distribution Statement: 1-Approved for public release; distribution is unlimited.
Acknowledged Federal Support: **Y**

RPPR Final Report
as of 04-Oct-2022

Publication Type: Journal Article Peer Reviewed: Y **Publication Status:** 1-Published
Journal: Soft Matter
Publication Identifier Type: Publication Identifier: 10.1039/C8SM01178H
Volume: 14 Issue: 29 First Page #: 6024
Date Submitted: Date Published:
Publication Location:
Article Title: Thermomechanical properties of monodomain nematic main-chain liquid crystal elastomers
Authors: Daniel R. Merkel, Nicholas A. Traugutt, Rayshan Visvanathan, Christopher M. Yakacki, Carl P. Frick
Keywords: Liquid crystal elastomer, rate-dependent behavior.
Abstract: Two-stage thiol-acrylate Michael addition reactions have proven useful in programming main-chain liquid crystal elastomers (LCEs). However, the influence of excess acrylate concentration, which is critical to monodomain programming, has not previously been examined with respect to thermomechanical properties in these two-stage LCEs. Previous studies of thiol-acrylate LCEs have focused on polydomain LCEs and/or variation of thiol crosslinking monomers or linear thiol monomers. This study guides the design of monodomain LCE actuators using the two-stage methodology by varying the concentration of mesogenic acrylate monomers from 2 mol% to 45 mol% in stoichiometric excess of thiol. The findings demonstrate a technique to tailor the isotropic transition temperature by 44 1C using identical starting monomers. In contrast to expectations, low amounts of excess acrylate showed excellent fixity (90.4 2.9%), while high amounts of excess acrylate did not hinder actuation strain (87.3 2.3%).
Distribution Statement: 1-Approved for public release; distribution is unlimited.
Acknowledged Federal Support: **Y**

Partners

,

I certify that the information in the report is complete and accurate:
Signature: Thao D. Nguy?n
Signature Date: 9/23/22 10:54AM

Liquid-crystalline elastomers (LCEs) are soft stimuli-responsive materials composed of stiff mesogens bound to an elastomeric network of flexible polymer chains. The mesogens can order and disorder in response to external stimuli, such as temperature and mechanical deformation. This allows LCEs to undergo reversible phase transitions between the polydomain, monodomain, and isotropic states. However, the motion of the mesogens relative to the polymer network also leads to unusual behavior, including a large reversible actuation in response to temperature and soft elasticity and enhanced dissipation. The latter includes an elevated loss factor (tan δ) over a wide range of frequencies and temperatures, and large hysteresis that increases with strain rate (Fig. 1). The viscoelastic properties of LCEs can be exploited to design transformative materials and structures with extreme dissipation behavior.

This project aims to develop a ***fundamental understanding*** of the relaxation mechanisms of main-chain LCEs to ***enable the design of extraordinary dissipation behaviors of LCE materials and structures*** over multiple length scales. We hypothesize that the enhanced dissipation behavior of LCEs arises from the coupling of the relaxation dynamics of the mesogens and polymer network and depends on the mesogen order and chain alignment. Furthermore, the intrinsic dissipation behavior can be exploited in an architected design to produce structures with extreme damping and energy absorption. The aims of the project are:

- Aim 1 Synthesize and characterize main-chain networks with tailored chain alignment and mesogen order
- Aim 2: Characterize the anisotropic relaxation behavior of the mesogens and polymer network using wide-angle X-ray scattering and LCEs with tailored structures.
- Aim 3: Develop a nonlinear thermoviscoelasticity theory for LCEs.
- Aim 4: Design, fabricate, and characterize architected LCE structures.

At the end of the fourth (final) year, we completed Aims 1 - 4. The outcomes for the Aims have been described in the prior years' annual reports and published in archival journals. This report collates the main results of the project shown in previous years' reports.

Aim 1.1 Synthesize and characterize the main-chain networks with tailored network and mesogen order.

A cornerstone of this research effort was to produce three sets of LCE networks with tailored network chain and mesogen order:

1. LCE 1 - Polydomain LCEs with randomly aligned chains and randomly aligned mesogen domains
2. LCE 2 - Monodomain networks with aligned chains
3. LCE 3 - Monodomain networks with unaligned chains

An illustration of the chemistries we've developed is shown in Fig. 1. This method gives us the option to create tailored LCE networks based on the spacer chosen. If the first spacer propanedithiol (C3) is chosen, polydomain LCEs (LCE 1) and monodomain networks with aligned chains (LCE 2) can be synthesized. In both cases, an excess amount of acrylate is used such that a sample can initially be synthesized through a Michael addition reaction and then photo-crosslinked to control alignment. For the LCE 1 sample, photo-crosslinking is performed in an unstretched state, while for the LCE 2 sample, photo-crosslinking is performed in a stretched state. The stretching process aligns both the mesogens and polymer chains, which are then stabilized via photo-

crosslinking. The LCE 3 sample can be synthesized by simply switching to spacer to allyl-dithiol, which enables reversible addition-fragmentation chain-transfer (RAFT). In this scenario, when the sample is stretched and photo-crosslinked, the RAFT reaction relaxes the polymer chains while the mesogens stay in an aligned state – thus producing the LCE 3 sample. The advantage of this chemistry is that LCEs can be synthesized in three unique states using virtually the same chemistry. The only difference between the spacers is an extra C=C double bond to enable the RAFT reaction in the LCE 3. This allows us to explore the influence of LCE structure with minimal variations in chemistry from sample to sample.

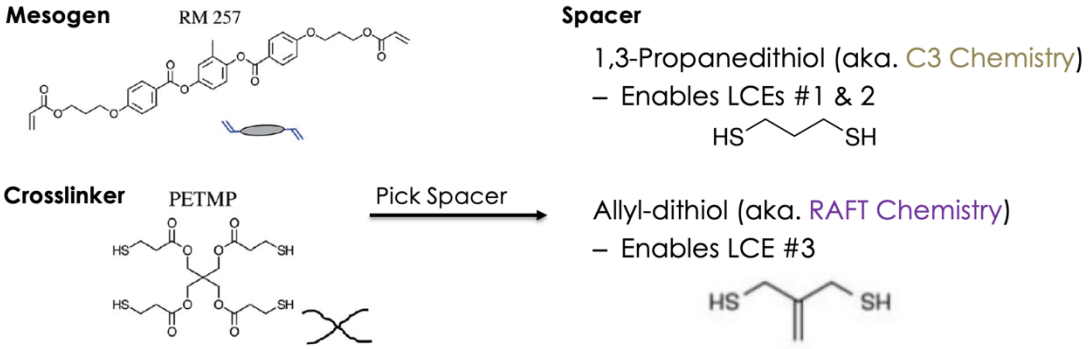

***Figure 1**. Chemistry used to create three LCE networks used in this study.*

We can compare the behavior of these two approaches using dynamic mechanical analysis (Fig. 2). In this experiment, both C3 and RAFT chemistries were tested before photo-crosslinking in the unstretched state. These results demonstrate that both spacers yield networks with very similar starting behavior.

We also discovered that the influence of liquid-crystal and network structure plays a significant role in the dissipative behavior of the networks (Fig. 3). In this experiment, we compared the thermomechanical response of a polydomain sample (LCE 1) to a monodomain sample with increasing chain alignment (LCE 2). If we focus on the behavior at Ti, the dynamic soft elasticity dip becomes more pronounced, and a secondary peak in the tan delta develops with increasing strain amounts. Although this plot is normalized from the glass transition (0) to the isotropic transition (1), these results demonstrate that the tan delta can approach a value of 2 at temperatures 60 to 70°C above the glass transition. These values of damping are unprecedented for elastomeric networks in the rubbery regime.

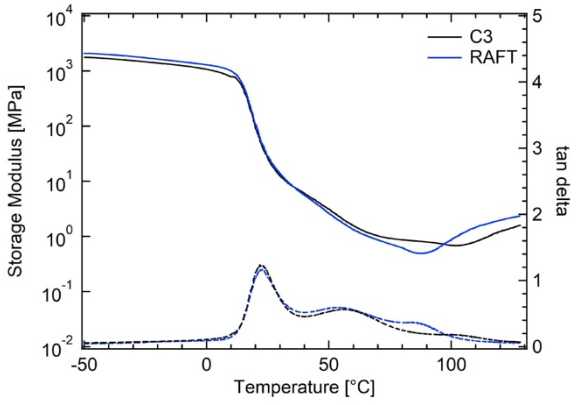

Figure 2. *DMA showing storage modulus and tan delta as a function of time for unstretched LCE networks using two different spacers. The glass transition for both networks is identical, while the dynamic soft elasticity dip (an indication of Ti) is within 14ºC.*

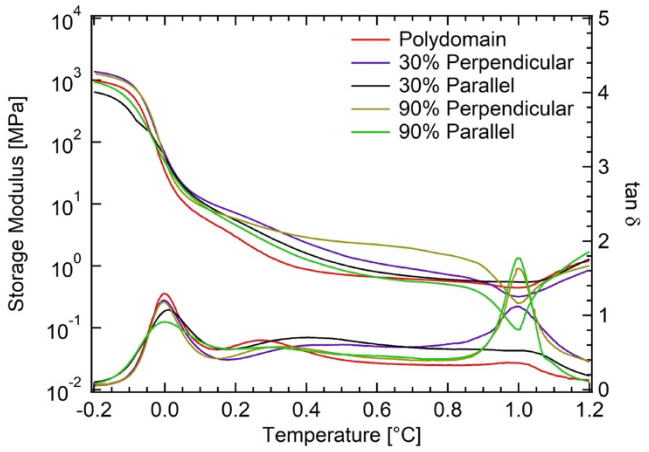

Figure 3. *Compare a polydomain LCE network (LCE 1) to an LCE network with aligned mesogens and chains (LCE 2). The LCE 2 networks were tested at two levels of programmed strain, 30 and 90%, and in two orientations – perpendicular or parallel to the direction of alignment.*

Aim 1.2 Characterize the effects of chemical structure, mesogen order, and network structure on the damping properties of LCE networks

In the prior year, we developed a uniaxial tensile test to measure the rate-dependent load-unload stress-strain response and investigate the effect of mesogen relaxation. We have completed testing of the C3 LCE networks prepared with different pre-strains, 0%, 30%, and 90%. The 30% strain corresponds with the onset of the polydomain-monodomain (P-M) transition, and the 90% strain corresponds with the end of the P-M change. In the following, we will refer to the 0%, 30%, and 90% pre-strained materials as polydomains, lightly aligned polydomains, and monodomains. Thin sheets of the polydomain networks were prepared as described in Aim 1.1. The strips were pre-stretched between 2 clamps to different strain levels,

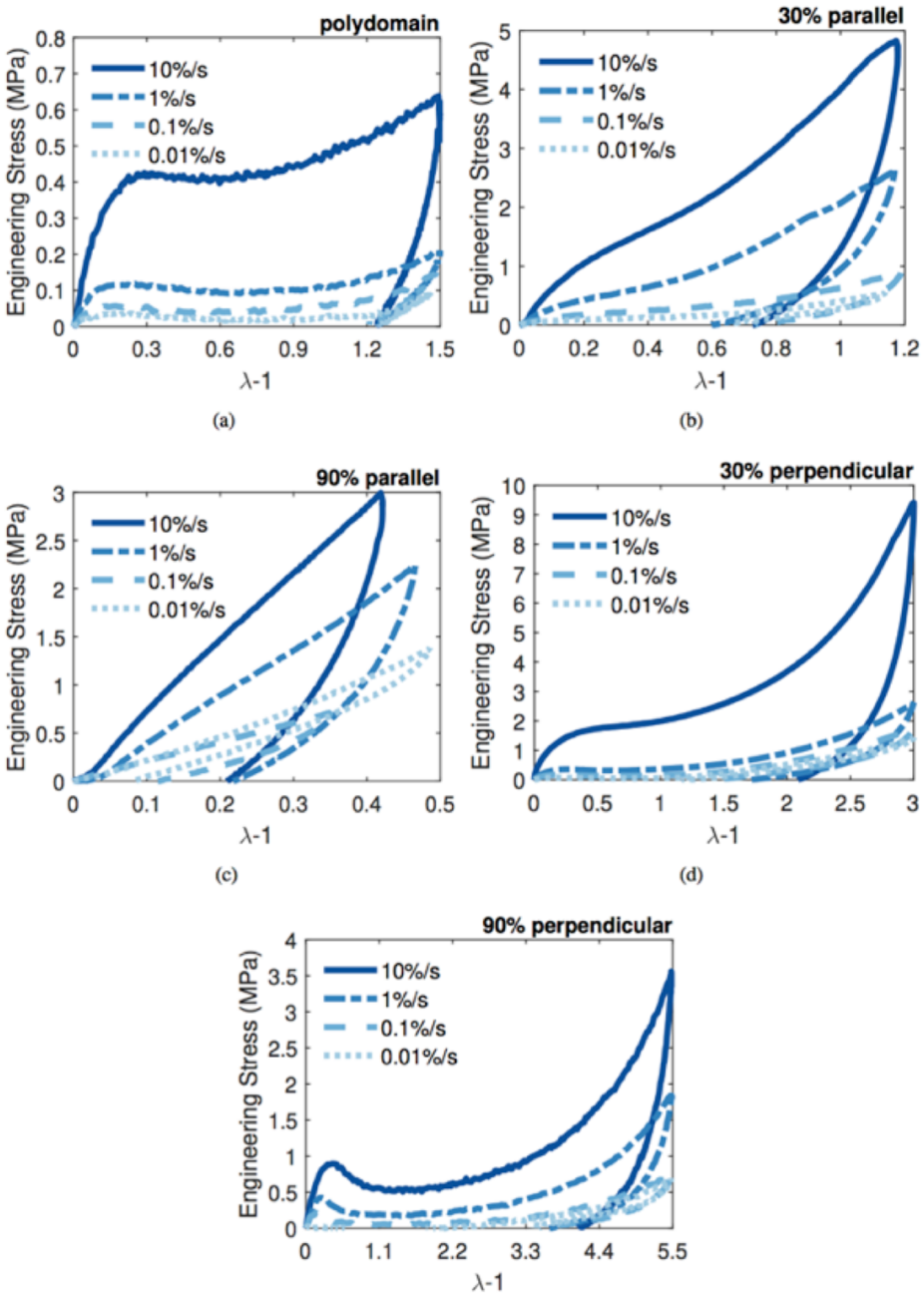

Figure 4. *The rate-dependent uniaxial tension stress-strain response for representative for different pre-stretched LCE networks and loading directions relative to the pre-stretched direction: (a) 0% polydomain, (b) 30% parallel, (c) 90% parallel, (d) 30% perpendicular, and (e) 90% perpendicular.*

0%, 30%, or 90% before being exposed to the second stage polymerization process to lock in the degree of alignment. Thin strips were cut from the pre-stretched sheets, and the strips were thermally rejuvenated at 125°C for 30 minutes before cooling to the test temperature and annealed for 15 minutes before being mounted in an MTS Insight 5 testing machine equipped with a 1 kN load cell. The central section of the specimen was speckled for 3D digital image correlation (DIC) by drawing a random pattern of dots using a black permanent marker.

The networks were stretched to different maximum stretch levels to measure the rate-dependent stress response. The maximum stretch levels were determined from preliminary tests to failure. The strips were subjected to displacement-controlled load-unload tests at different engineering strain rates ranging from 0.01%/s to 10%/s. One specimen was prepared for each network and loading direction relative to the pre-stretched direction and tested at all strain rates to reduce the effect of specimen-to-specimen variability. The force response was measured by the MTS load cell and divided by the undeformed cross-sectional area of the strip to calculate the engineering stress. The engineering strain was calculated from the grip-to-grip displacements. The Young's modulus was calculated by fitting the slope of the engineering stress-strain curve for strains less than 10%. The hysteresis was computed by numerically integrating the area under the engineering stress-strain curve.

The specimens were imaged during loading by two monochrome cameras arranged in stereo. A commercial 3D-DIC program, VIC-3D (Correlated Solutions), was used to analyze the images of the deforming specimen to calculate the 3Ddisplacement field and the in-plane strain fields. These were used to examine the development of heterogeneities in the strain field from mesogen relaxation.

The stress response of all LCE networks loaded both parallel and perpendicular to the alignment direction exhibited noticeable strain rate-dependence and inelastic deformation upon unloading (Fig. 4). The polydomain and aligned networks loaded perpendicular to the alignment direction displayed a soft stress response, characterized by a rate-dependent initiation stress, followed by a strain-softening response, and a strain-stiffening response. For the 90% pre-stretched material loaded at 0.01%/s strain rate, we did not detect a linear region before the initiation of the soft stress response.

The Young's modulus and hysteresis for all LCE networks and loading directions exhibited a power-law increase with strain rate (Fig. 5). The power-law exponent was obtained by linear regression of the log-log plot with respect to strain rate. The Young's modulus and hysteresis for the monodomain had a noticeably smaller power-law exponent than the polydomain and lightly aligned network. The modulus of the monodomain was larger and less rate-dependent along the alignment direction. The hysteresis was higher along the perpendicular direction. These results indicated that alignment stiffened the material and decreased the sensitivity to strain rate.

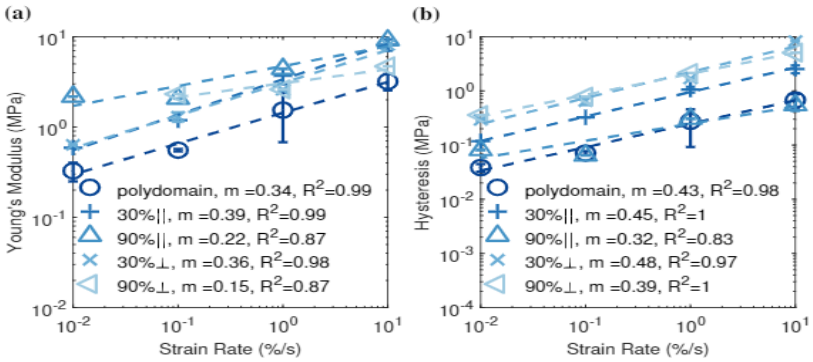

Figure 5. *The (a) Young's modulus and (b) hysteresis of the uniaxial tension stress response for the different networks and loading directions exhibit a power-law dependence on the strain rate. Plotted are the averages over the repeated tests, and the error bars indicate the variation between repeated tests. The m is the slope of a linear fit of the log-log plot.*

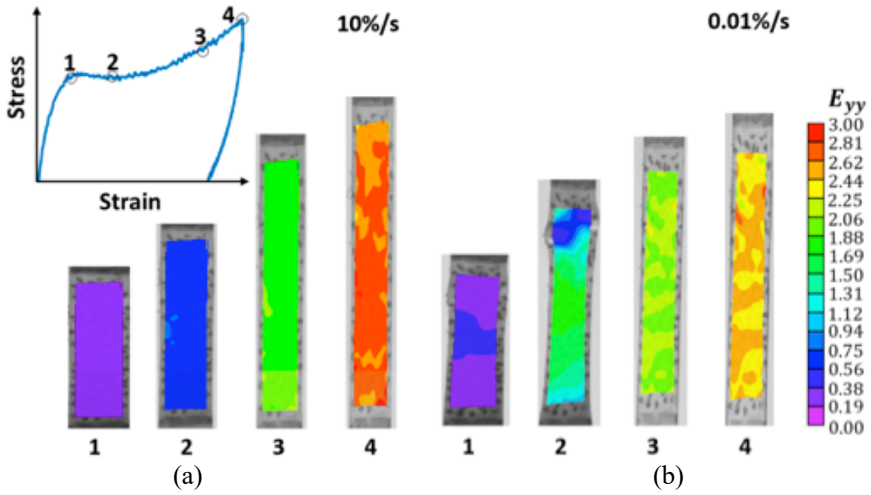

Figure 6. *The Green-Lagrange axial strain Eyy from 3D-DIC for representative tests of the polydomain samples at (a) 10%/s and (b) 0.01% strain rates showing the development of heterogeneities in the strain field from mesogen relaxation.*

Results from 3D-DIC showed that all specimens experienced the development of a non-uniform strain field during the uniaxial tension test. Fig. 6 shows the axial Green-Lagrange strain field measured using 3D-DIC for representative tests of poly-domain specimens at the highest and lowest strain rates. For all strain rates, the strain field appeared uniform until the initiation of the soft stress response. At the lower strain rates, 0.01%/s and 0.1%/s, the initiation of the soft-stress response corresponded to the appearance of a band of higher strains in the middle of the specimen. Subsequent strain-softening of the stress response was accompanied by the development of additional bands of lower strains, producing a pattern of alternating bands of higher and lower strains towards the end of the soft stress region.

To more quantitatively characterize the development of strain heterogeneities, we calculated the standard deviation of the Green-Lagrange axial strain. We plotted for all specimens and strain rates the standard deviation in strain normalized by the average strain (Fig. 7). For the polydomain, the standard deviation was initially small, indicating a uniform strain response. The normalized strain variation began to grow after the initiation of the soft stress response and became maximum near in the soft-stress region before decreasing back to near zero. Larger strain variability was measured for slower strain rates, which confirmed that the strain variability was caused by domain relaxation. Little strain variability was observed for the 10%/s strain rate, which suggests that the characteristic relaxation time for domain relaxation was on the order of 10-100s.

The normalized strain variability was initially high for the aligned specimens. The pre-straining process caused the development of a non-uniform domain structure that led to a non-uniform strain response upon unloading. For the samples loaded in the perpendicular direction, the normalized variability decreased until the initiation of the soft stress response, where it increased and became maximized in the soft-stress region. The development of the strain variability was less sensitive to the strain rate for the monodomain specimens, and the normalized variability for the 0.01%/s was nearly

identical to that for the 10%/s loading rate. This suggests that mesogen relaxation is characterized by smaller relaxation times.

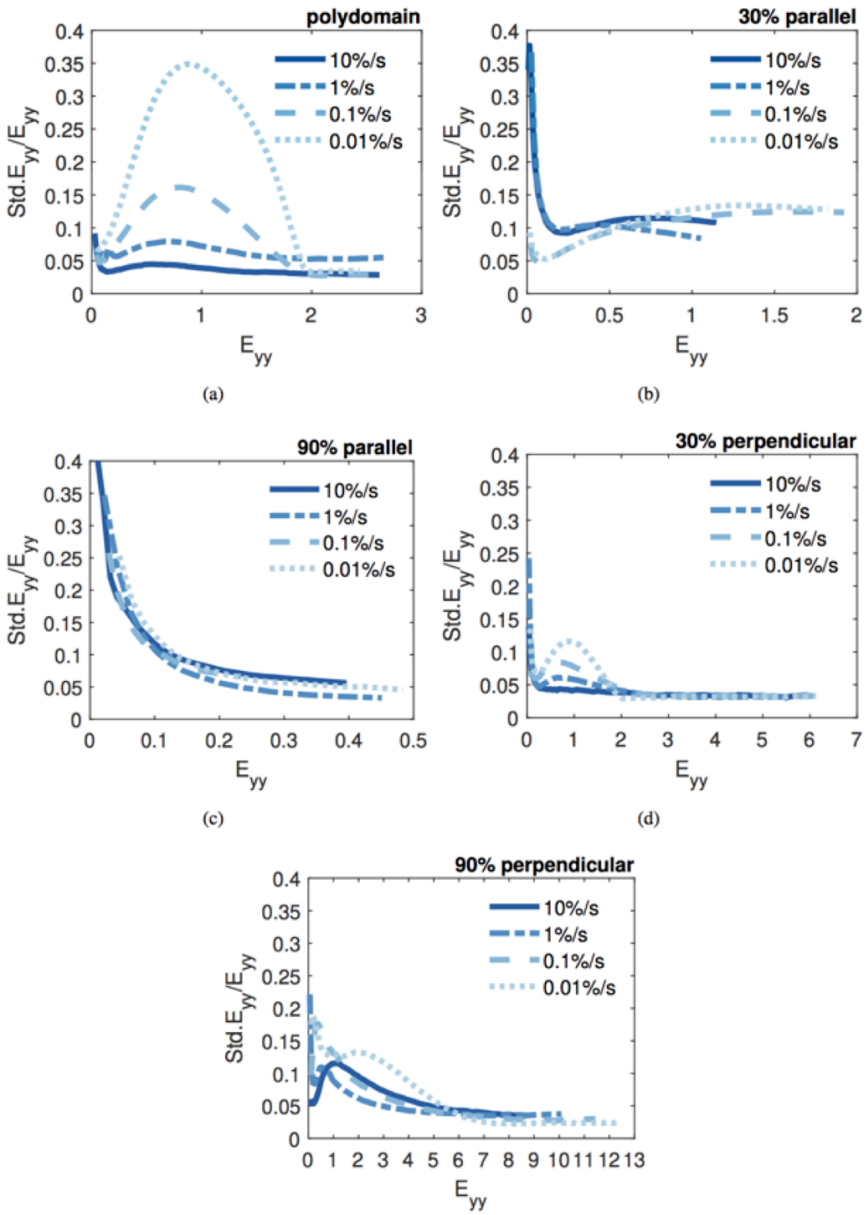

Figure 7. *The standard deviation of the Green-Lagrange axial strain Eyy from 3D DIC normalized by the specimen-averaged Eyy for representative tests at different strain rates for the different LCE network structures and loading directions: (a) 0% polydomain, (b) 30% parallel, (c) 90% parallel, (d) 30% perpendicular, and (e) 90% perpendicular.*

Aim 2: Characterize the anisotropic relaxation behavior of the mesogens and polymer network using wide-angle X-ray scattering and LCEs with tailored structures.

A major emphasis of Aim 2 was to determine the amount of order established in networks with tailored alignment. This helps us to determine the amount of strain we should use when (a) programming alignment of mesogens and (b) determining

relaxation behavior. Wide-angle X-ray scattering (WAXS) 2D plots can be seen in Fig. 8. For both chemistries tested, unstretched polydomain samples show diffuse halos. With increasing amounts of strain, both chemistries go from a diffuse halo to showing 2 distinct bright spots separated by 180°, which indicates nematic order in liquid crystals.

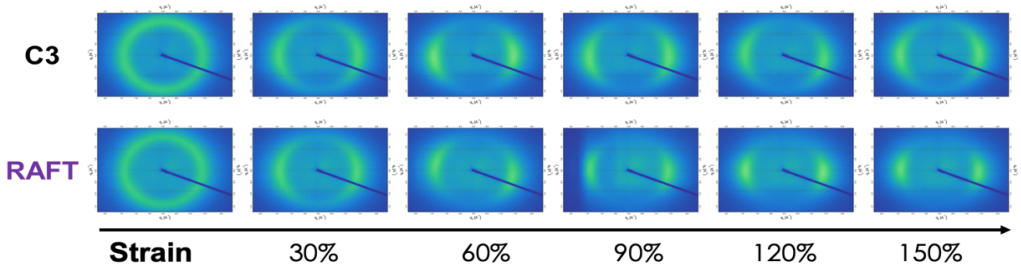

Figure 8. *2D WAXS plots showing the chemistries transition from polydomain mesogen ordering to nematic monodomains with increasing amounts of strain.*

We can quantify the amount of nematic order by using the 1D WAXS profiles (Fig. 9). Order parameter (S) can be calculated by fitting these curves and integrating them using the following equation.

$$S = \frac{\int_0^{\pi/2} I(\gamma)\frac{3\cos^2\gamma - 1}{2}\sin\gamma d\gamma}{-\frac{1}{2}\int_0^{\pi/2} I(\gamma)\sin\gamma d\gamma}$$

Overall, 30% strain induces a limited amount of order with S = 0.43, while 90% strain yields an order parameter of S = 0.58. Further increasing strain does not improve the order parameter of the liquid crystals. This finding is important to this study, so we can systematically link low, moderate, and high amounts of liquid crystal order to strain.

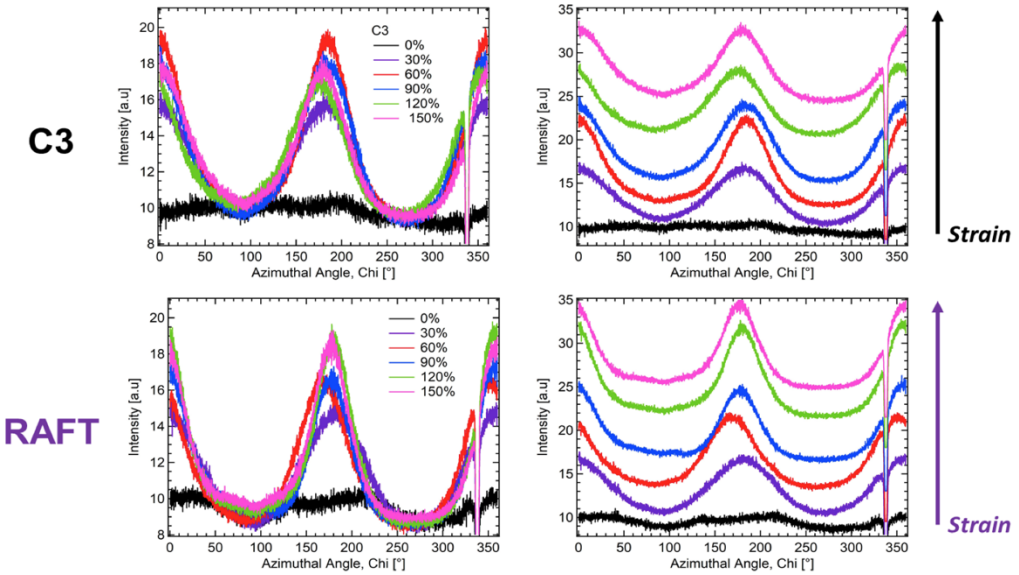

Figure 9. *The orientation distribution of scattering intensity for polydomain networks subjected to different stretches.*

Aim 3 Develop a nonlinear viscoelastic theory for LCEs (Nguyen)

Experiments in Aim 1 showed that the large deformation uniaxial tension behavior of the acrylate main-chain LCEs was highly anisotropic, rate-dependent, and exhibited large hysteresis and inelastic strain upon unloading [1]. Stretching a monodomain in a direction perpendicular to the director produced an initial linear viscoelastic response, followed by a peak stress and strain-softening, which indicates mesogen rotation towards the loading direction, then strain stiffening, which indicates stretching of the polymer network. The linear region, soft stress region, and large-deformation strain-stiffening were highly rate-dependent. Stretching parallel to the director produced a highly viscoelastic elastomeric response that exhibited significant rate-dependence and hysteresis.

To capture these features of the viscoelastic behavior, we developed a nonlinear viscoelastic micropolar theory for nematic elastomers that incorporated the mechanisms of viscous director rotation and viscoelastic network deformation. We focused on the case of nematic elastomers with a monodomain microstructure and assumed that the order parameter is unaffected by deformation, such that the microstructure is described by a director $\mathbf{d}$ in the current configuration and $\mathbf{d}_0$ in the reference nematic configuration. This allows us to conceptualize the material as a micropolar continuum characterized by a deformation field and a single director field $\mathbf{d}(\mathbf{x})$ in the current configuration. Following the developments of Del Piero,[1] we can derive the balance of linear momentum for the Cauchy stress tensor $\boldsymbol{\sigma}$ and the balance of angular momentum for the stress couple tensor $\mathbf{M}$,

$$\boldsymbol{\nabla}_{\mathbf{x}}\boldsymbol{\sigma} + \mathbf{b} = \mathbf{0},$$
$$\boldsymbol{\nabla}_{\mathbf{x}}\mathbf{M} + \mathbf{c} + 2\boldsymbol{\omega}^{\boldsymbol{\sigma}} = \mathbf{0},$$

where $\mathbf{b}$ is the body force, $\mathbf{c}$ is the body force couple, and $\omega_k^{\sigma} = \frac{1}{2}\varepsilon_{ijk}\sigma_{jk}$ is the axial vector of the skew of the Cauchy stress.

To describe the time-dependent viscoelastic behavior, we assume that the deformation gradient can be decomposed into elastic and viscous parts,

$$\mathbf{F} = \mathbf{F}^{\boldsymbol{e}}\mathbf{F}^{\boldsymbol{v}},$$

where $\mathbf{F}^{\boldsymbol{v}}$ is treated as the internal state variable of the material system.

The free energy density, in general, is assumed to be a function of the external and internal variables as,

$$W = \widehat{W}(\mathbf{F}, \mathbf{F}^{\boldsymbol{e}}, \mathbf{d}, \boldsymbol{\nabla}\mathbf{d}, \mathbf{d}_0).$$

Note that W depends on the internal variable $\mathbf{F}^{\boldsymbol{v}}$ through $\mathbf{F}$ and $\mathbf{F}^{\boldsymbol{e}}$. Furthermore, we assume that the stress and stress couple can generally be split into a quasistatic component that does not depend on the objective rate of $\mathbf{d}^{\circ}$ nor the objective rate of $\boldsymbol{\nabla}\mathbf{d}^{\circ}$ and a viscous component that can depend on both,

$$\boldsymbol{\sigma} = \boldsymbol{\sigma}^{0}(\mathbf{F}, \mathbf{F}^{\boldsymbol{e}}, \mathbf{d}, \boldsymbol{\nabla}\mathbf{d}, \mathbf{d}_0) + \boldsymbol{\sigma}^{\boldsymbol{v}}(\mathbf{F}, \mathbf{F}^{\boldsymbol{e}}, \mathbf{d}, \boldsymbol{\nabla}\mathbf{d}, \mathbf{d}^{\circ}, \boldsymbol{\nabla}\mathbf{d}^{\circ}, \mathbf{d}_0),$$
$$\mathbf{M} = \mathbf{M}^{0}(\mathbf{F}, \mathbf{F}^{\boldsymbol{e}}, \mathbf{d}, \boldsymbol{\nabla}\mathbf{d}, \mathbf{d}_0) + \mathbf{M}^{\boldsymbol{v}}(\mathbf{F}, \mathbf{F}^{\boldsymbol{e}}, \mathbf{d}, \boldsymbol{\nabla}\mathbf{d}, \mathbf{d}^{\circ}, \boldsymbol{\nabla}\mathbf{d}^{\circ}, \mathbf{d}_0).$$

Following the arguments of Coleman and Noll[2] and Coleman and Gurtin[3], we can develop thermodynamic restrictions for the constitutive relations for the quasistatic stress and stress couple as,

$$\boldsymbol{\sigma}^{0} = \frac{1}{J}\left(\frac{\partial W}{\partial \mathbf{F}}\mathbf{F}^{\mathrm{T}} + \frac{\partial W}{\partial \mathbf{F}^{\mathrm{e}}}\mathbf{F}^{\mathrm{eT}} - \boldsymbol{\nabla}\mathbf{d}^{\mathrm{T}}\frac{\partial W}{\partial \boldsymbol{\nabla}\mathbf{d}}\right)$$

$$\mathrm{skew}[\boldsymbol{\sigma}^0] = -\frac{1}{J}\mathrm{skew}\left[\frac{\partial W}{\partial \mathbf{d}} \otimes \mathbf{d} + \frac{\partial W}{\partial \boldsymbol{\nabla}\mathbf{d}}\boldsymbol{\nabla}\mathbf{d}^{\mathrm{T}}\right],$$
$$\mathbf{M}^0 = \frac{1}{J}\left(\mathbf{d} \times \frac{\partial W}{\partial \boldsymbol{\nabla}\mathbf{d}}\right),$$
$$\mathrm{sym}[\boldsymbol{\sigma}^v] = 0.$$

Some interesting results arise from this general formulation. First, the viscous stress for director rotation is skew. For the case of a homogenous director field, $\boldsymbol{\nabla}\mathbf{d} = \mathbf{0}$ and $\boldsymbol{\nabla}\mathbf{d}^{\circ} = \mathbf{0}$. Then, from the above constitutive relations, $\mathbf{M}^0 = \mathbf{0}$. It can be shown from the thermodynamic restrictions that $\mathbf{M}^{\boldsymbol{v}} = \mathbf{0}$, which causes $\mathrm{skew}[\boldsymbol{\sigma}^0] = \mathbf{0}$ from the angular momentum causes. The constitutive relations above reduce to

$$\boldsymbol{\sigma}^0 = \frac{1}{J}\left(\frac{\partial W}{\partial \mathbf{F}}\mathbf{F}^{\mathrm{T}} + \frac{\partial W}{\partial \mathbf{F}^{\mathrm{e}}}\mathbf{F}^{\mathrm{eT}}\right),$$
$$\mathrm{skew}[\boldsymbol{\sigma}^0] = -\mathrm{skew}[\boldsymbol{\sigma}^v] = -\frac{1}{J}\mathrm{skew}\left[\frac{\partial W}{\partial \mathbf{d}} \otimes \mathbf{d}\right].$$

To satisfy the positive dissipation inequality, we choose the following constitutive equations for the viscous director stress,

$$\mathrm{skew}[\boldsymbol{\sigma}^v] = \eta_D(\mathbf{d} \otimes \mathbf{d}^{\circ}), \qquad \mathbf{d}^{\circ} = \dot{\mathbf{d}} - \mathbf{W}\mathbf{d},$$

where $\mathbf{W}$ is the spin tensor. The rate of dissipation from viscous director rotation is then $\eta_D\|\mathbf{d}^{\circ}\|^2$. Noting that $\mathrm{sym}[\boldsymbol{\sigma}^v] = 0$, the total stress can be written as,

$$\boldsymbol{\sigma} = \frac{1}{J}\left(\frac{\partial W}{\partial \mathbf{F}}\mathbf{F}^{\mathrm{T}} + \frac{\partial W}{\partial \mathbf{F}^{\mathrm{e}}}\mathbf{F}^{\mathrm{eT}}\right) + \frac{\eta_D}{2}(\mathbf{d} \otimes \mathbf{d}^{\circ} - \mathbf{d}^{\circ} \otimes \mathbf{d}).$$

Combining the above equations for $\mathrm{skew}[\boldsymbol{\sigma}^v]$ and $\mathrm{skew}[\boldsymbol{\sigma}^0]$ and rearranging terms gives an evolution equation for the director,

$$\dot{\mathbf{d}} = \mathbf{W}\mathbf{d} - \frac{1}{J\eta_D}\left(\frac{\partial W}{\partial \mathbf{d}} - \left(\frac{\partial W}{\partial \mathbf{d}} \cdot \mathbf{d}\right)\mathbf{d}\right).$$

The η_D is the viscous resistance to director rotation, and we will refer to it as the director viscosity. Similarly, we choose the following constitutive equation for the viscous velocity gradient to satisfy the positive dissipation criteria,

$$\mathbf{L}^{\boldsymbol{v}} = \frac{1}{\eta_N}\mathbf{F}^{\mathrm{eT}}\frac{\partial W}{\partial \mathbf{F}^{\mathrm{e}}}$$

The η_N is the viscous resistance to the elastomeric network deformation, and we will refer to it as the network viscosity. At equilibrium, $\mathbf{F}^{\boldsymbol{e}} = \mathbf{1}$, $\mathbf{d}^{\circ} = \mathbf{0}$ and $\boldsymbol{\sigma}^{\boldsymbol{v}} = \mathbf{0}$. Then we recover the constitutive relations for the equilibrium elastic behavior of the material.

$$\boldsymbol{\sigma} = \frac{1}{J}\left(\frac{\partial W}{\partial \mathbf{F}}\mathbf{F}^{\mathrm{T}}\right),$$
$$0 = \frac{\partial W}{\partial \mathbf{d}}(\mathbf{I} - \mathbf{d} \otimes \mathbf{d})$$

To demonstrate the capabilities of the theory, we apply the following free energy density,

$$W = \underbrace{-\frac{\mu^{\mathrm{eq}}}{2}\bar{\lambda}\ln\left(1 - \frac{I_N - 3}{\bar{\lambda}}\right)}_{W^{\mathrm{eq}}} \underbrace{-\frac{\mu^{\mathrm{neq}}}{2}\bar{\lambda}\ln\left(1 - \frac{I_N^e - 3}{\bar{\lambda}}\right) - \mu^{\mathrm{neq}}\ln(J^e)}_{W^{\mathrm{neq}}} - p(J-1),$$

where J=det[$\mathbf{F}$] is the volumetric deformation, p is the Lagrange multiplier of the incompressibility the constrain $J=1$. The $I_N = \mathrm{trace}[\mathbf{l}_0\mathbf{F}^{\mathrm{T}}\mathbf{l}^{-1}\mathbf{F}]$ is the mechanical stretch of the network and $I_N^{\mathrm{e}} = \mathrm{trace}[\mathbf{l}_0\mathbf{F}^{\mathrm{eT}}\mathbf{l}^{-1}\mathbf{F}^{\mathrm{e}}]$ is the elastic part responsible to the time-dependent response. The remaining are model parameters: $\bar{\lambda}$ is the locking stretch, which marks the onset of rapid strain-stiffening; μ^{eq} is the equilibrium shear modulus; and $\mu^{\mathrm{eq}} + \mu^{\mathrm{neq}}$ is the instantaneous shear modulus. The step length tensors in the current and reference are given by,

$$\boldsymbol{l} = r^{-\frac{1}{3}}(\mathbf{I} - \mathbf{d} \otimes \mathbf{d}) + r^{\frac{2}{3}}\mathbf{d} \otimes \mathbf{d},$$
$$\boldsymbol{l}_0 = r^{-\frac{1}{3}}(\mathbf{I} - \mathbf{d}_0 \otimes \mathbf{d}_0) + r^{\frac{2}{3}}\mathbf{d}_0 \otimes \mathbf{d}_0,$$

where r is a material parameter related to the order parameter. Finally, we assume an Eyring-type (i.e., stress-activated) model for the director viscosity based on experimental measurements of the strain-rate dependence of the peak stress[4],

$$\eta_D = \eta_{D0} \exp\left(-\frac{\boldsymbol{\sigma}:\boldsymbol{\sigma}}{k_S}\right).$$

where η_{D0} is the intrinsic directory viscosity and k_S is the activation energy.

We next chose representative material parameters for the model based on our previous work's rate-dependent uniaxial tensile tests.[5] The anisotropic step length ratio r=5.83 was determined from the monodomain's wide-angle x-ray scattering (WAXS) measurement. The η_{D0} = 40 MPa·s and k_S = 0.7 MPa^2 were fit to the draw stress at strain rates 0.1/s and 0.01/s. The instantaneous shear modulus $\mu^{eq} + \mu^{neq}$=1.5 MPa was determined from the Young's modulus assuming incomprehensibility, while μ^{eq} = 0.25 MPa, $\bar{\lambda}$ = 5.7, η_N = 800 MPa·s was fit to the large deformation network response.

We applied the model to simulate the uniaxial tension stress response. Figure 10 shows a comparison between experiments and simulations. The model captured the loading curve at a strain rate of 10^{-1}/s and the rate-dependence of the linear and soft stress region. However, the model over-predicted the peak stress at the beginning of the stress response and underestimated the hysteresis. This is likely because we only used one relaxation process for director rotation and one for network deformation.

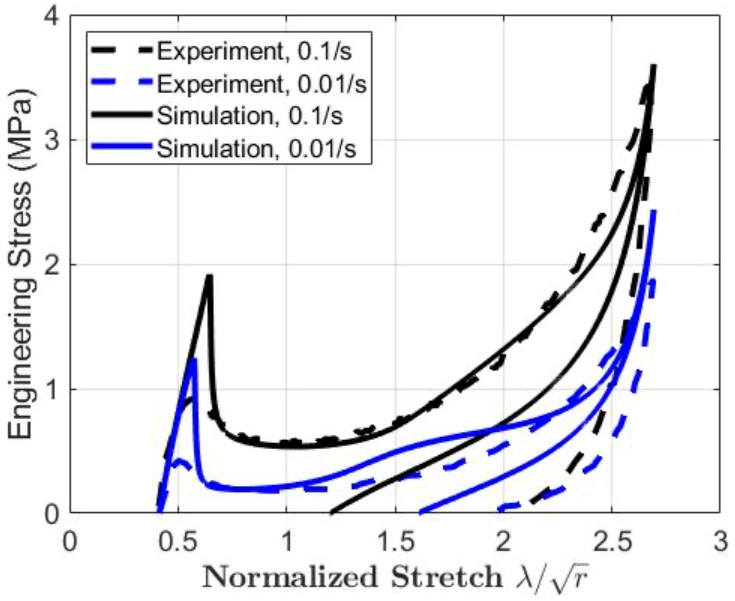

Figure 10. *Uniaxial tension response of LCE at 0.1/s and 0.01/s, with director perpendicular to applied loading initially. In general, the modeling results showed good agreement with experimental measurements of the uniaxial tension stress response*

Finally, we performed a parametric study to determine the effect of the material parameters on the stress response (Fig. 11). The parameters r, θ_0 for the angular orientation of the reference director relative to the loading direction, locking stretch $\bar{\lambda}$, director viscosity η_D, and network viscosity η_M were varied one by one. The results shown in Figure 2 clearly show the physical significance of each parameter and their distinct effects on the uniaxial loading and unloading stress response of the nematic elastomer. The anisotropic ratio of the step lengths r determines the end strain of the soft stress region and the permanent strain upon unloading. The locking stretch $\bar{\lambda}$ determines the strain at which significant strain stiffening of the network response occurs. The network viscosity η_M controls the hysteresis of the network stress response. Furthermore, the director viscosity η_D and the activation energy k_s determine the rate-dependent soft-stress plateau and the strain for the onset of the stress response. Finally, the stress overshoot is determined by η_D, k_s, and the initial orientation of the director relative to the loading direction.

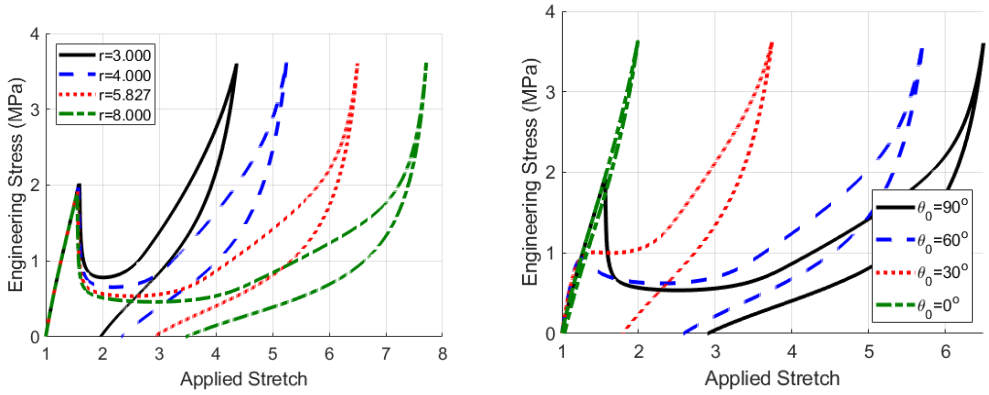

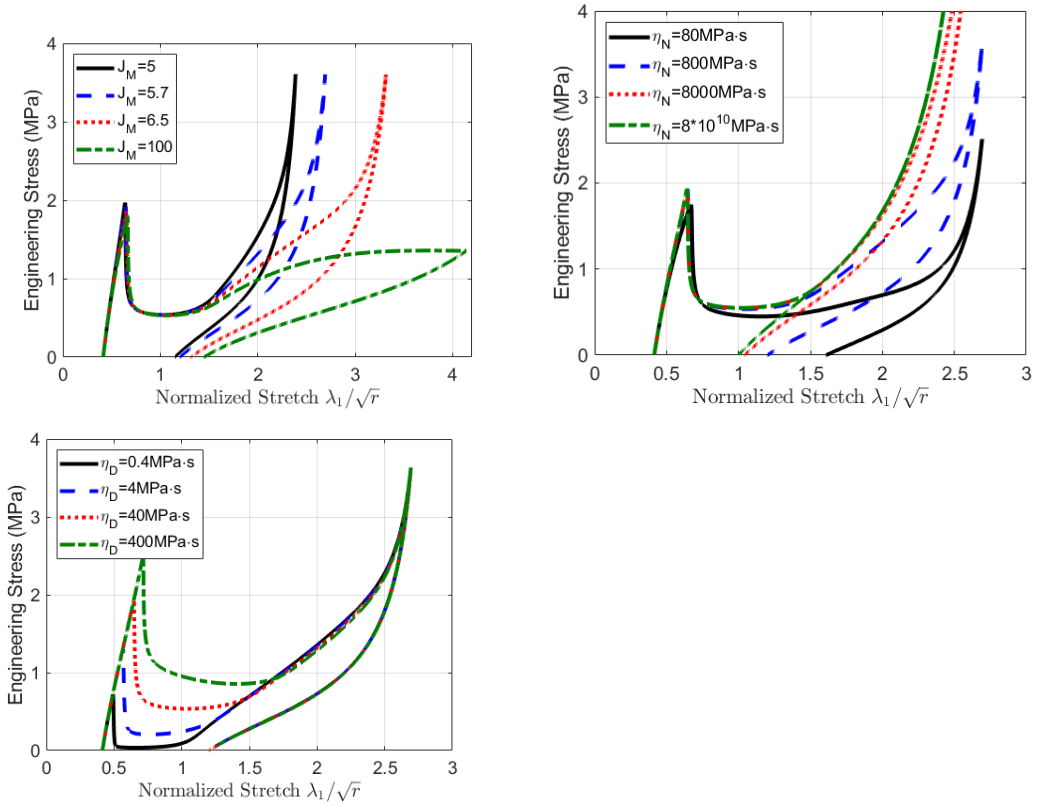

Figure 11*. From upper left to lower right, increasing r increases the end strain of the soft stress response and the permanent strain upon unloading. Decreasing the reference director orientation from* $\theta_0 = 90^o$ *decreases the initial stress overshoot. Increasing the locking stretch* $\bar{\lambda}$ *increases the strain at which strain stiffening occurs. Increasing the network viscosity increases the network relaxation time. For this range of* η_M*, the network changes from an equilibrium response with little hysteresis (*$\eta_M = 80$*) to an instantaneous response also with little hysteresis (*$\eta_M = 8e10$*). The largest dissipation occurs for* $\eta_M = 800$*. Increasing* η_D *increases the stress in the semi-soft regime and the onset strain of the semi-soft region.*

The study thus far shows that the nonlinear viscoelasticity theory can reproduce many key features of the loading and unloading response. The results demonstrated that the network viscoelastic deformation and director viscoelastic rotation affect different regions of the load-unload stress response. The model has a small number of parameters, most of which have distinct effects on the stress-strain curve.

Aim 4: Design, fabricate and characterize architected LCE structures (Kang, Yakacki)

Based on the previous findings that architected LCEs show intriguing power-law relations between the specific energy absorption and strain rate and the power-law exponent can be modulated by controlling the mesogen alignment, we pursued a deeper understanding of the interaction between LCE units by vertical stacking of unit cells. We investigated stacked LCE structures by arranging polydomain LCE units as 2×n arrays (2 columns, n rows). Figure 12a shows a series of experimental snapshots of a 2×2 stacked structure with polydomain LCE under compressive

loading at a strain rate of 2.38×10^{-2} (1/s). Firstly, both layers collapse downward simultaneously until a certain point ((i) to (ii)). Then, the bottom layer slightly recovers while the top layer keeps collapsing downward ((ii) to (iii)). Lastly, both layers collapse downward till fully deformed ((iii) to (iv)). The reaction force as a function of displacement of 2×2 stacked LCE structures at different strain rates is given in Figure 12b. For each strain rate, two force peaks correspond to the collapse of two vertical layers. As the strain rate increases, the reaction force increases correspondingly, indicating a strong strain rate dependency. We also studied taller 2×3 and 2×4 stacked structures. The specific energy absorption of stacked LCE structures from 2×1 to 2×4 are plotted at different strain rates (Figure 12c). The specific energy increased with the stacking number, which was not observed for elastic materials, and it is beneficial for impact protection applications. The dependence on strain rate and the stacking number originates from the viscoelastic behavior of LCEs.

To understand the energy absorption density increase, we simulated the stacked structures and evaluated the contributions of the stored energy and dissipated energy to the specific energy absorption for different stacks. The specific energy, dissipated, and stored energy are plotted as a function of the number of stacks at a strain rate of 2.27×10^{-4} (1/s), as shown in Figure 12d. As the number of stacks increases, the dissipated energy keeps increasing while the stored energy remains roughly constant. Therefore, the specific energy (the sum of dissipated and stored energy) increased with the number of stacks. The buckling of one layer caused the other layers to recover (i.e., straighten) and then buckle again after the initial buckled layer collapsed. This load-unloading cycle increased the viscoelastic dissipation without changing the stored energy.

To investigate whether energy absorption can be further enhanced by varying geometry of stacked LCE structures, the beam thicknesses were gradually increased from top to bottom layers while keeping the overall volume the same as the uniform thickness cases (from top to bottom: thinnest to thickest, thickness variation between adjacent layers was 0.05 mm). Figure 12e plots the reaction force as a function of displacement for the 2×8 structures with uniform beam thickness and varying beam thickness. The variation in the beam thickness causes the layers to collapse layer-by-layer from top to bottom, producing 8 peaks in the force-displacement curve. In contrast, the layers collapsed simultaneously when the beam thickness was uniform, and the force response did not have 8 distinct peaks corresponding to 8 vertical layers. The area underneath the force-displacement curve (energy absorption) shows that the structure with varying thickness absorbed more energy than with uniform thickness.

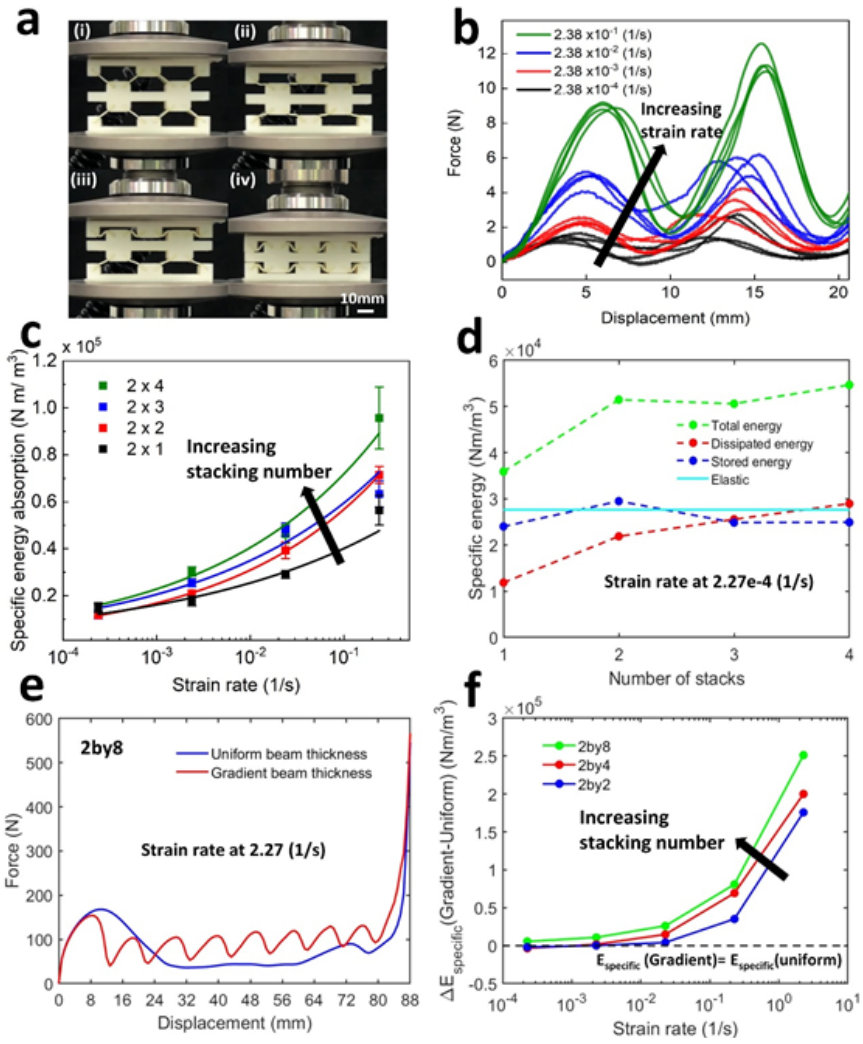

Figure 12. *Mechanical energy absorption through stacked LCE structures. a) Experimental snapshots of a 2×2 stacked LCE structure (two unit cells in series) under compressive loading at a strain rate of 2.38×10^{-2} (1/s): (i)-(ii) initially both layers collapse simultaneously, (ii)-(iii) the bottom layer slightly recovers back while the top layer keeps collapsing, (iii)-(iv) both layers collapse till fully deformed. b) Force-displacement curves of 2×2 stacked LCE structures at different strain rates. Different curves for the same color represent multiple samples. c) Specific energy absorption of stacked LCE structures plotted as a function of strain rates at a different number of stacks from 2×1 to 2×4. d) Specific total, dissipated, and stored energy of stacked LCE structure and specific stored energy of stacked elastic structure plotted as a function of a number of stacks at a strain rate of 2.27×10^{-4} (1/s). For the elastic material, the modulus was equal to the equilibrium part of the polydomain LCE. e) Force-displacement curves of 2×8 stacked LCE structures for both uniform and gradient beam thickness at a strain rate of 2.27 (1/s). f) Specific energy difference between gradient and uniform cases for 2×2, 2×4, and 2×8 stacked LCE structures plotted as a function of strain rates. The horizontal dash line passing through zero indicates the case where the specific energy of the gradient case is equal to that of the uniform case.*

To quantitatively compare gradient with uniform structures, the specific energy difference between gradient and uniform cases at different strain rates is given in Figure 12f. For both 2×4 and 2×2 structures, the specific energy difference between gradient and uniform increases with strain rates and stays above zero, indicating that gradient structures absorb more energy than uniform cases at higher strain rates. This

is because the layers of the uniform structures tended to collapse simultaneously at higher strain rates. In contrast, the layers of the gradient structures collapsed sequentially. The sequential collapse of the layers caused the LCE beams to unload and reload, which produced more viscous dissipation. The difference in the specific energy between gradient and uniform structures increased with the number of stacks from 2×2 through 2×4 to 2×8 at higher strain rates. It implies that more dissipation from more loading cycles was generated with a larger number of stacks.

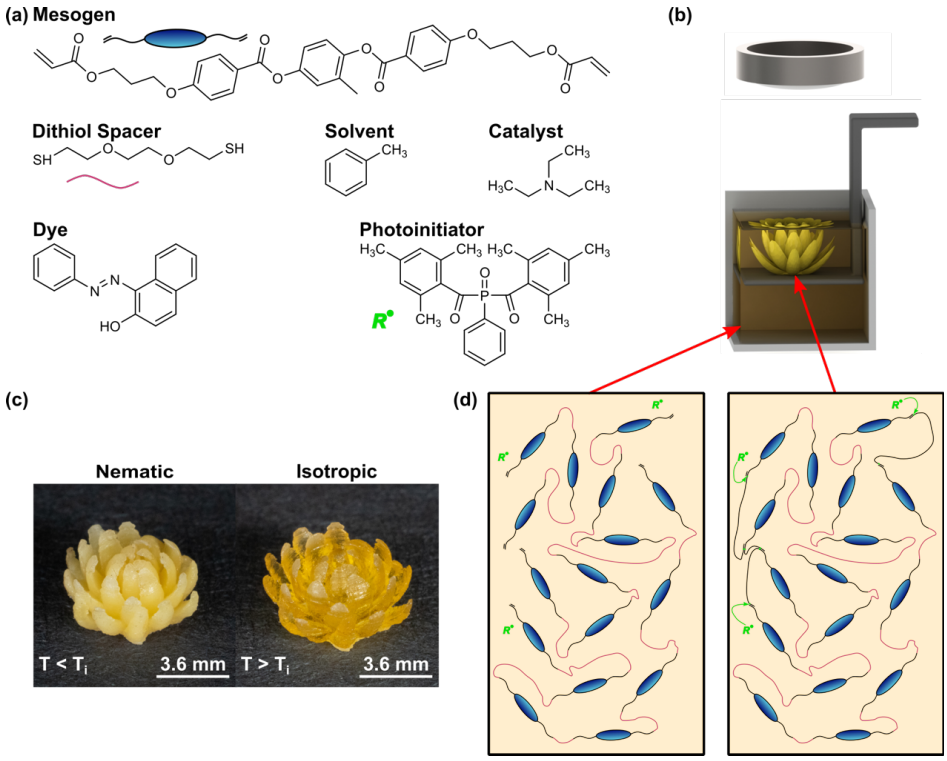

Figure 13 *A liquid crystal resin is created using the chemical structures shown in (a), starting with a Michael addition reaction using the liquid crystal mesogen, RM257, flexible dithiol spacer, EDDET, and addition catalyst, TEA, in a melt with an organic solvent, toluene. The photoinitiator, PPO, is added to allow photocuring during printing, and the photo-absorptive dye, Sudan I, is used to prevent overexposure during printing so high-detailed print features can be achieved. A rendering of the printer setup is shown in (b). A sample print is shown in (c) and shows the LCEs can be nematic at room temperature (left) and isotropic when heated (right). An illustration of the oligomer solution before (left) and after (right) photocuring are shown in (d). Photocuring the oligomers during printing creates cross-linking bonds between acrylate terminal groups.*

In summary, the study shows that vertically stacking LCE units with uniform beam thickness can increase specific energy absorption as the number of stacks increases, which is not observed in elastic materials. The stacking effect originates from specific dissipated energy increasing with the number of stacks due to partial unloading or recovery and oscillations of deformed beams. In addition, we could further enhance the energy absorption performance of stacked LCE structures by introducing a gradient in the beam thickness to produce a sequential collapse of the bilayers. In this work, we used LCE to fabricate tilted beams for a simple one-dimensional metastructure, but further enhancement of energy absorption is expected through

systematic structural design in the future. We envision our findings contribute to the fundamental understanding of the nonlinear energy absorption mechanisms of architected LCE structures and applications where lightweight and extreme energy absorption are desirable, such as aerospace and automotive vehicles and personal protection.

We developed a method to 3D print architected designs using light processing (DLP). An illustration of the DLP setup can be seen in Figure 13. Using this technique, we can produce polydomain structures with micron-sized features (Figure 13c). It should be noted that this is the first demonstration of bulk LCE structures being 3D printed with DLP. We compared the rate dependence of two elastomeric material test cubes, one made from LCEs and the other from TangoBlack (Figure 14). The DLP-printed LCE samples maintained a high degree of rate dependence compared to the TangoBlack elastomer. The Tg's of the LCE sample was measured at -6.6°C, while TangoBlack was measured at ~14°C. Figure 13b showed that even though the TangoBlack had a Tg closer to ambient test conditions, the LCE materials demonstrated a more significant increase in rate dependence when increasing the compressive deformation rate from 0.02 mm/s to 20 mm/s.

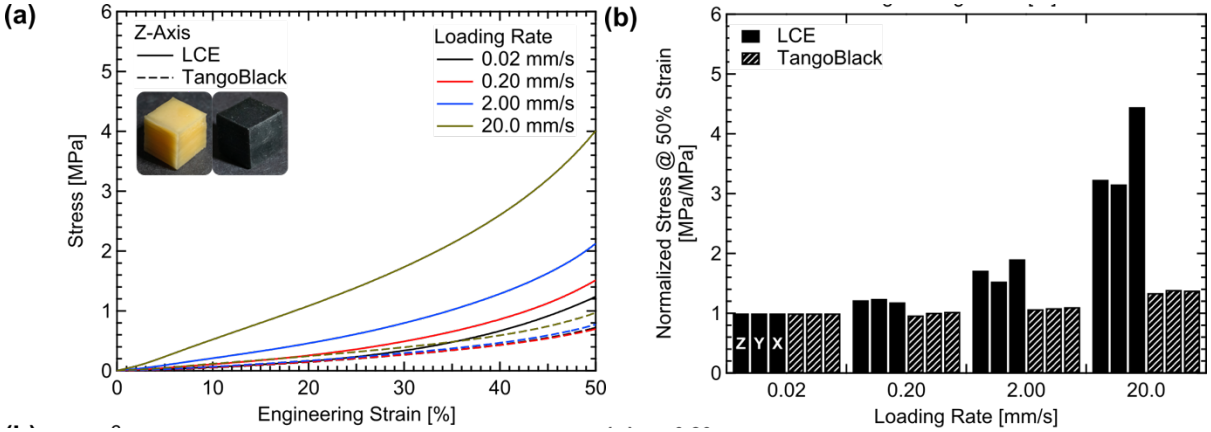

Figure 14 *- DLP 3D printed LCE and TangoBlack cubes were tested under uniaxial compressive loading. The stress-strain results for testing on the z-axis are shown in (a), where you can see an increased stress response in the LCE cube as the loading rate is increased. Comparatively, the TangoBlack appears to follow the same stress responses, regardless of loading rate. The normalized stress at 50% strain of each cube was observed to quantify rate dependence for the two materials in (b). By comparison, the LCE exhibits a greater rate dependence than TangoBlack. The print direction doesn't significantly impact the material properties of either sample.*

As a next step, a DLP-printed lattice structure was printed to demonstrate the feasibility of this approach. A representative Kelvin lattice is shown in Figure 15d. This lattice was scaled in a way to demonstrate anisotropic behavior. The lattice was then compressed along all 3 axes individually to show a difference in test direction and rate dependence. Finally, we characterized the energy absorption properties of 3D-printed LCE lattices. Figure 16 compares the LCE lattice from Figure 15 to an equal TangoBlack lattice (designated Lattice 1). The energy under the load-unloading curve was calculated at a loading rate of 20 mm/s. Overall, the LCE lattice demonstrated a large hysteresis response compared to TangoBlack for all orientations tested. Overall, our success in DLP printing of LCEs gives us greater control to design and fabricate architected structures.

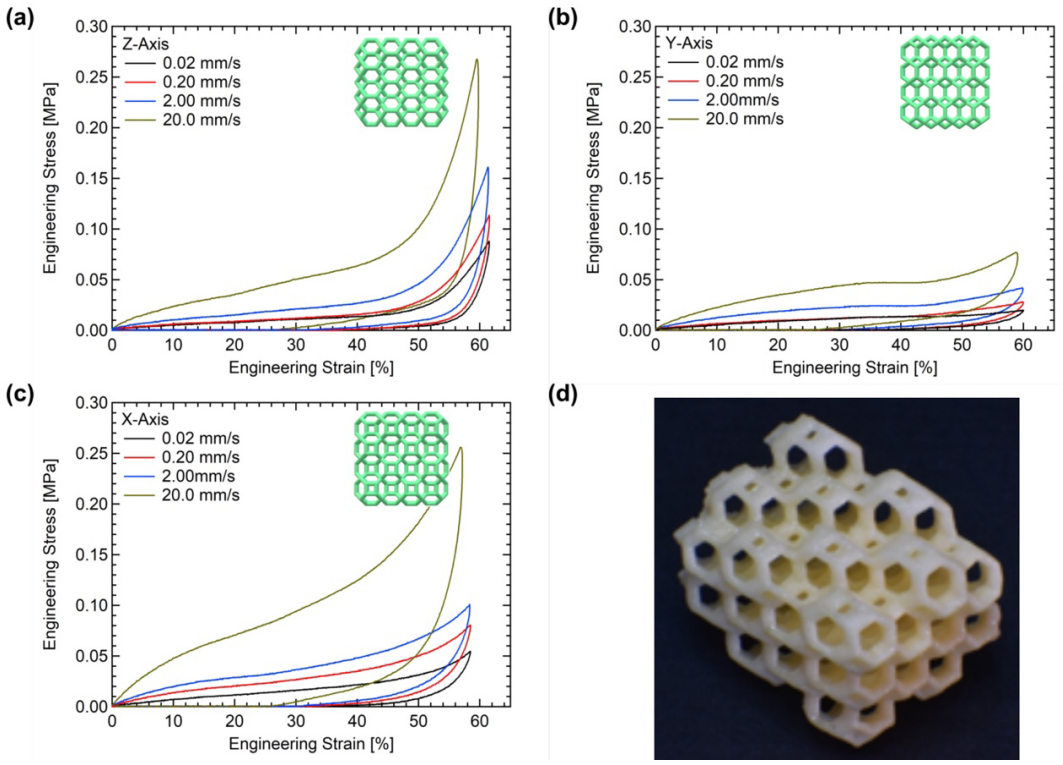

Figure 15 *- Compressive stress-strain data for a DLP printed LCE lattice structure (Lattice 1). Tests were done on each axis at four different speeds, beginning at 0.02 mm/s and increasing an order magnitude up to 20.0 mm/s. Testing shows that the material exhibits stiffer mechanical responses with greater rates of strain. The stress-strain curves for the z-axis (a), y-axis (b), and x-axis (c) show that the lattice structure exhibited different stress-strain responses to the uniaxial testing for each axis. (d) Photo of a representative sample of Lattice 1 measuring ~10 mm in height.*

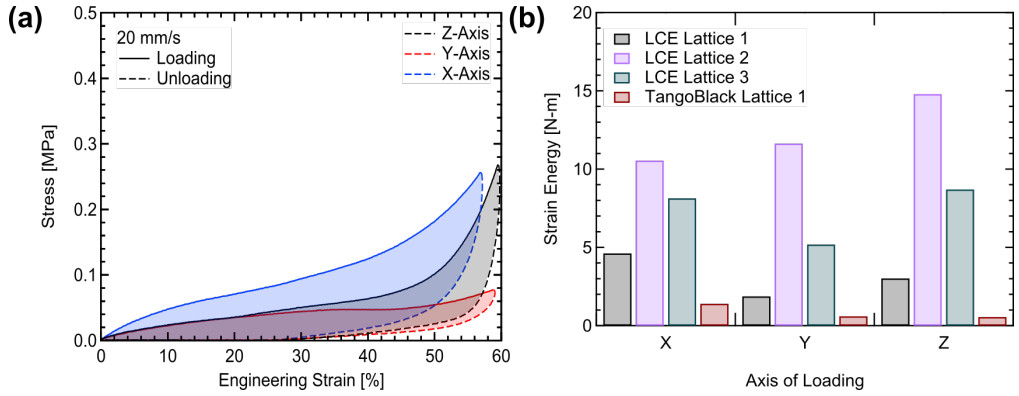

Figure 16. *(a) A representative plot of how the energy absorbed by the LCE lattice was calculated using the loading-unloading curve. (b) A comparison of Lattice 1 compressed in the X, Y, and Z axes for LCE and TangoBlack materials. Lattices 2 and 3 are alternative lattices that have been fabricated but not yet compared to TangoBlack.*